# Land Subsidence in the Mekong Delta Derived From Advanced Persistent Scatterer Interferometry With an Infrastructural Reference Network

Nils Dörr , Andreas Schenk , and Stefan Hinz

*Abstract*—**The Vietnamese Mekong Delta (VMD) has been affected by environmental challenges for several decades, including coastal erosion and land subsidence. Subsidence rates of several cm/yr have been reported in parts of the delta, which are one order larger than the regional sea level rise of 3.3 mm/yr. The precise monitoring of subsidence with high spatial and temporal resolution is essential to understand its causes and associated risks, and to support the development and monitoring of countermeasures. Here, we present subsidence estimates between 2017 and 2022 derived from advanced persistent scatterer interferometry (PSI) applied to Sentinel-1 data. The PSI approach fully integrates temporary persistent scatterers, in order to derive the best possible persistent scatterer network for long time series. Furthermore, we adapted a method to optimally integrate reference points with known displacement to suppress spatially correlated nuisance (SCN) in the derived displacement time series. Due to a lack of geodetic references, we built an infrastructural reference network based on large bridges with piled foundations of about 70 m depth, which are only affected by compaction in deeper soil layers. We compare the method with the standard referencing approach in PSI, and show that referencing to the selected reference bridges with our method enables to measure the largest part of the subsidence while reducing the SCN considerably. We find the highest subsidence rates of more than 7 cm/yr mainly in urban areas, and various kinds of temporal nonlinearities.**

*Index Terms*—**Interferometric synthetic aperture radar (InSAR), land subsidence, Mekong Delta, persistent scatterers, reference network, Sentinel-1.**

## I. INTRODUCTION

### A. Motivation

LAND subsidence is a global geological phenomenon with manifold causes [1], [2], [3], [4], [5], [6]. It can have direct consequences in the form of structural damage [7], [8] as well as indirect environmental consequences as a result of the accelerated relative sea level rise, like an increased vulnerability of the affected area to salinization of water resources [9], [10], flooding [11], [12], [13], erosion [14], and permanent inundation. Latter problems particularly concern coastal areas, such as

sinking river deltas. [15] showed that the world's river deltas were inhabited by 339 million people in 2017, and [16] found that land subsidence exceeded rates of global sea level rise in 18 of 33 representative deltas. Fast sinking coastal areas are especially concentrated in Southeast Asia, and in most cases characterized by rapidly growing populations, thus by significant increases in groundwater extraction and loading from construction activities [17], [18]. Prominent examples are Bangkok, Jakarta, and the VMD, where rates of up to 12 cm/yr [7], [19], 10 cm/yr [11], and 6 cm/yr [20], [21], [22] have been reported. The latter are one order of magnitude larger than the regional sea level rise of about 3.3 mm/yr [23].

The VMD represents the southern part of Vietnam and lies on average 0.8 m above sea level [24]. It is home to about 17 million people and of large economical importance due to the rice production and aquafarming [25]. The delta has recently been affected by different environmental challenges, including a decrease in sediment supply due to climatological [26] and anthropogenic causes in the form of dam construction in the upper Mekong [27]. Further challenges are due to increasing riverbank and coastal erosion [28], as well as saltwater intrusion into surface- and groundwater [29], [30].

A major problem is the mentioned land subsidence, which has been affecting the VMD for more than 15 years. It has been mainly attributed to groundwater overextraction [20], [21], [31], as well as the natural compaction of young Holocene deposits [32], which might be accelerated by additional loading due to the recently intensive construction activity [33]. The VMD consists of a complex stratification of marine and alluvial deposits from the Miocene and Holocene, which are in total 300–400 m thick on average and overlie a Mesozoic basement [34]. The aquifer-aquitard system is described in detail in [35], and comprises seven confined aquifers and aquitards with spatially varying thicknesses. Well logs and hydrogeological models suggest that the aquitards are heterogeneous and at least partly disconnected [31], [36], [37], resulting in a potential hydraulic connection between the aquifers [38]. The confined aquifers have been affected by increasing groundwater extraction since the 1990s, leading to continuously decreasing hydraulic heads [20], [34], [35]. While households mainly use unlicensed wells to pump from shallow Pleistocene aquifers for daily needs and small businesses, licensed wells for commercial purposes pump from deeper aquifers [38]. The exact number of unlicensed wells is unknown, however, Danh and Khai [39]

stated that there are more than one million shallow tube wells in the VMD. Hoan et al. [34] estimated in a modeling study that the by far largest pumping rates and storage changes in the south-western VMD are found in the upper-middle Pleistocene aquifer at 80–151 m depth, followed by the middle Pliocene aquifer at 183–276 m depth.

The geodetic monitoring of surface movements, preferably with a high spatial and temporal sampling rate, is crucial for investigating the causes and associated risks of land subsidence and supporting the development and monitoring of reasonable countermeasures. Measured subsidence time series are used to analyze spatial and temporal characteristics of the subsidence and help to better understand the underlying geology and drivers of the subsidence. Different geodetic tools have been used to measure subsidence [1]. A preferred method nowadays is space-borne multitemporal interferometric synthetic aperture radar (MT-InSAR) such as the PSI [40], [41], as it is characterized by high spatial sampling, large coverage and usually a temporal sampling rate of several days, which is sufficient for many geoscientific applications.

### B. Article Contribution

MT-InSAR approaches are characterized by limitations regarding long-term and large-scale monitoring. In this work, we present results of the recent land subsidence between 2017 and 2022 in the VMD based on advanced Sentinel-1 PSI. The results represent an update of the subsidence rates presented in [20] and [22], which included rates from the periods 2006–2010 and 2014–2019, respectively. We adapted the PSI approach from [42], which also incorporates temporary persistent scatterers (TPSs) into the PSI approach, for robust large-scale PSI monitoring. TPSs are coherent only in one or several segments of the studied time series, and can be caused by different drivers such as construction activities, natural decorrelation over time or floods. Their integration into PSI leads to a significant gain in the number of identified measurement points, which increases with increasing time series length, as shown in [43].

Large-scale monitoring with interferometric synthetic aperture radar (InSAR) is challenging in study areas with very turbulent conditions in the troposphere, leading to high uncertainty in the displacement estimates at large distances to the spatial reference [44]. These conditions are found in the VMD due to its coastal and low-latitude location and flat topography. We here present and apply a covariance-based reference integration method, adapted from [45], to suppress SCN in the estimated displacement time series of measurement points. The method exploits measurements at reference locations with known displacement time series to sample the SCN and interpolates the sampled noise onto all other pixels, considering its spatial statistics. We use a network of infrastructural reference objects with negligible displacements, for lack of a well distributed network of permanent global navigation satellite system (GNSS) stations in the study area, which would represent an optimal reference network for the proposed method. The selected objects are large bridges with deep piled foundations. Dörr et al. [46]

showed that large bridges are statistically more stable than their surroundings, indicating that the largest part of the subsidence originates from shallow layers above their foundation depth. Here, an initial set of large bridges was automatically tested for negligible subsidence based on various statistical tests, and the selected bridges were finally used as reference objects.

### C. Related Work

Erban et al. [20] presented the first delta-wide subsidence estimates by means of ALOS PALSAR InSAR for the time period of 2006–2010, which showed subsidence rates of up to 4 cm/yr over large regions. They compared the measured InSAR rates with modeled compaction rates from a 1-D hydrogeological model. The model was based on measured hydraulic head drawdown rates in different aquifers, which averaged to 26 cm/yr among the delta. Measured and modeled subsidence results agreed well at head drawdown monitoring stations, and they concluded that the measured subsidence can be attributed to groundwater overexploitation, which leads to a compaction of the clay units that form the aquitards. These findings were supported by [31], who developed a delta-wide 3-D hydrogeological model with an integrated subsidence module. Their model showed an average subsidence of about 18 cm across the delta between 1991 and 2015 with increasing subsidence rates, which amounted to more than 2.5 cm/yr in 2015. Minderhoud et al. [33] showed on the basis of the results from [20] that the highest subsidence rates are found in land use classes with high human impact, further indicating anthropogenic causes of subsidence.

A more recent Sentinel-1 InSAR study with data acquired between November 2014 and January 2019 was conducted by the company GISAT in the framework of the Copernicus Emergency Management Service [22]. The results from that study exhibit subsidence rates of up to 5 cm/yr, with the largest rates mainly found in urban areas. Furthermore, they show more variability at short distances compared to the rather smoothed results by [20]. In general, differential subsidence on short distances can be related to many factors, including the loading of structures, previous land cover/land use, local geology, different foundation depths of buildings, etc. Wit et al.[8] studied differential subsidence in three cities across the VMD and showed that examined buildings with deep foundations going down to 50 m showed on average lower subsidence rates than their surroundings. The results coincide with the findings of [46], who studied differential subsidence between large bridges, which are usually built with a deep piled foundation, and their surroundings. This indicates significant compaction in shallow sediment layers above the foundation depth of these buildings.

First results from three subsidence monitoring stations on the Ca Mau peninsula were presented in [21] which measured depth-dependent soil layer settlement with regard to benchmarks situated in 100 m depth. The maximum subsidence rate from these monitoring stations was 31 mm/yr, which is almost three times larger than their roughly estimated settlement rate of ~13 mm/yr in layers below 100 m. They also attributed the measured subsidence to groundwater over-exploitation.
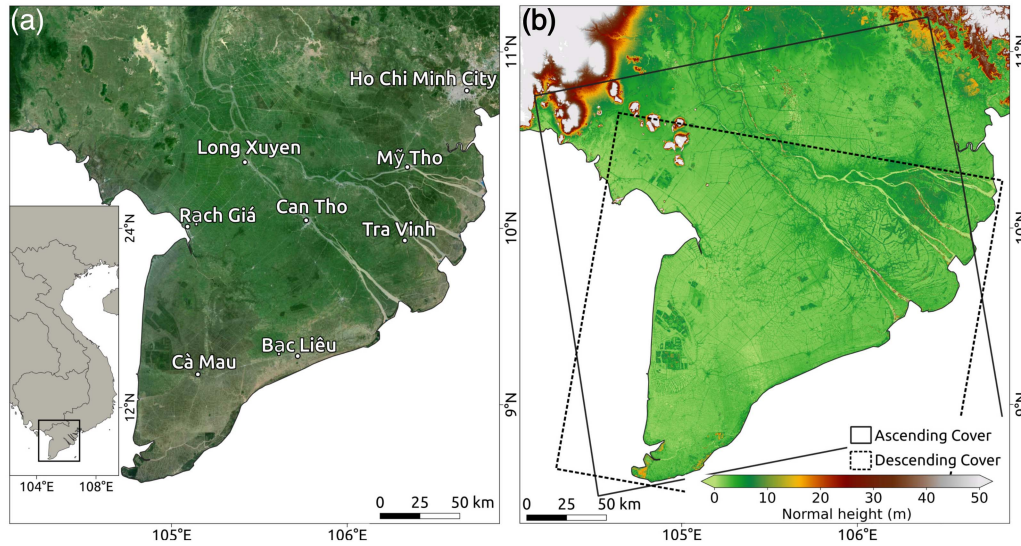
Fig. 1. (a) Optical satellite image composite and location of the VMD with names of important cities. Imagery data: Google Earth, 2024 Maxar Technologies. (b) Normal height in the VMD calculated with the global TanDEM-X 90 m DEM [47] and the EGM2008 gravitational model [48]. The covered areas of the exploited descending and ascending tracks are also displayed. We processed the overlap of both orbit tracks.
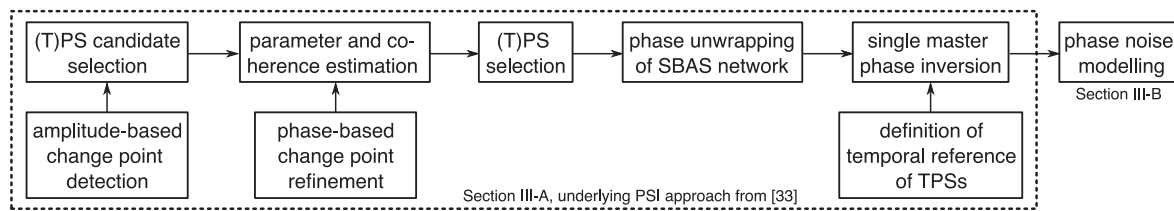


Fig. 2. Flowchart of the first part of the PSI approach, which is described in Sections III-A and III-B. The flowchart of the second part of the approach is displayed in Fig. 3 and described in Section III-C.

## II. DATA

We used 277 and 115 VV-polarized Sentinel-1 scenes, which were acquired between 2017 and 2022 over the VMD in descending and ascending orbits, respectively. An optical satellite image, the normal heights of the study area and the coverage of both orbit tracks are displayed in Fig. 1. We processed the overlap of both orbit tracks. The acquisitions were recorded in the interferometric wide swath mode. The interferometric preprocessing, which was carried out using ESA's SNAP software and comprised the joint coregistration of the synthetic aperture radar (SAR) scenes by means of enhanced spectral diversity [49] and the removal of the simulated reference and topographic phase based on the global TanDEM-X 90 m digital elevation model (DEM) [47]. The master acquisitions of the descending and ascending stacks are February 1, 2021 and December 22, 2020, respectively. The local time at descending and ascending acquisitions was 5:45 A.M. and 6:11 P.M., respectively.

## III. METHODS

We adapted the PSI approach described in [42], which combines the analysis of persistent scatterers (PSs) and TPSs, for robust large-scale displacement monitoring. In the following, we will first recap the main concepts of the PSI approach and subsequently describe the developed modifications.

### A. Overview of the Underlying PSI Method

The PSI approach from [42], which is referred to as multi-small baseline subset approach (M-SBAS), is characterized by following steps: 1) identification of PS and TPS candidates; 2) parameter and temporal coherence estimation; 3) PS and TPS selection; 4) joint phase unwrapping of PSs and TPSs (see Fig. 2). A special feature of M-SBAS is that the parameter estimation, which comprises the estimation of the height, linear displacement rate and thermally induced displacement rate of (T)PS candidates, is carried out sequentially instead of simultaneously, which is usually done in PSI. This way, the computational cost is reduced from $\mathcal{O}^3$ to $3\mathcal{O}$. However, this causes phase contributions of the unconsidered parameters to potentially disturb the estimation of the parameter of interest in each estimation step. Two approaches are included in the algorithm to tackle this problem: 1) the use of different small-baseline subsets in each parameter estimation; 2) the application of an iterative parameter estimation.

TPSs are scatterers which are coherent only in one or several subsegments of the studied time series. Their identification can be described as a change point detection problem. The selection of TPS candidates is based on amplitude statistics. The underlying assumption is that significant changes in a pixel's temporal coherence are accompanied by significant changes in its amplitude. Pixels are selected as TPS candidates if different

segments of their amplitude time series can be described by different Rayleigh distributions. The change point detection is realized with a sequential F-Test procedure, which was originally described in [50].

Dörr et al. [42] found that the initial change point detection based on amplitude statistics can be inaccurate. They showed examples of appearing TPSs at new constructions whose estimated appearing date coincided with the start of constructions. However, the temporal coherence of these scatterers only increased significantly when the constructions were finished. For this reason, the initially estimated change points of TPS candidates are reestimated during the iterative parameter estimation using a phase-based likelihood-ratio-test.

The joint unwrapping of selected PSs and TPSs is realized with SNAPHU [51] within the Stanford method for persistent scatterers (StaMPS) software [52]. A small-baseline network is unwrapped in order to prevent TPSs whose lifetime does not include the master scene from being excluded from the analysis. After the unwrapping, a single-master phase inversion step is carried out, which includes TPSs being referenced to neighboring pixels with similar displacement time series if their lifetime does not enclose the selected master scene.

### B. Modeling of Phase Noise

Phase noise affects the performance of InSAR-based displacement monitoring. Relevant SCN contributions are tropospheric and ionospheric delays [53], [54], orbital errors [55], [56], and surface displacements, which are not the target of the specific displacement monitoring. The latter include tidally induced displacements [57], [58], plate motions [59], [60], and possibly displacements due to atmospheric pressure loading and pole tides. Even if phase variations of these effects are negligible across the studied area, their absolute offsets in interferograms can lead to significant phase ramps in ground range direction due to the mapping onto the local line-of-sight (LOS).

We implemented the modeling of three phase noise terms in addition to the existing functionality in StaMPS. They include: 1) an improved tropospheric delay modeling based on the ERA-5 weather reanalysis and the approach proposed by [61]; 2) the consideration of solid Earth tides and displacements due to ocean tide loading, making use of the tidal models *solid* [62] and *SPOTL* [63], respectively; 3) tectonic plate motions, based on Euler pole information of the Sunda plate from the NNR–MORVEL56 model [64], following the approach by [60]. All unconsidered or insufficiently modeled phase noise terms are summarized as residual noise and considered in the following strategy to reduce residual SCN.

### C. Reference Integration for Spatially Correlated Noise Suppression

Residual SCN persists in interferograms due to insufficient noise modeling and unconsidered noise signals. The former can be due to the limited performance of numerical weather models based on tropospheric delay modeling, which depends on the location of the study area [65], [66]. It decreases with decreasing latitude, decreasing topography in the study area and increasing

proximity to the coast due to higher water vapor content and variability in the atmosphere.

Various strategies have been proposed to account for SCN in interferograms or estimated displacement fields. One approach is to fit and subtract linear or quadratic spatial functions [67], [68], but this is not applicable if large-scale displacements are of interest. Another approach is the application of spatio-temporal filters, with the assumption that SCN is mostly spatially correlated, while temporary uncorrelated, and displacements are temporary and spatially correlated. However, such filters are characterized by several disadvantages. The selection of the filter parameters is nontrivial and should be based on the statistical properties of the atmosphere [69]. Furthermore, these filters are not able to estimate the tropospheric delays properly when the SAR sampling leads to the aliasing of daily and seasonal tropospheric variations [70]. Eventually, displacement signals might be temporarily uncorrelated, such as displacements from volcano deformation and earthquakes. In general, separating the atmospheric delays and displacements by means of a temporal filter is not possible in the case that their temporal correlation lengths overlap.

Alternatively, ground truth or reference displacement measurements such as from GNSS can be exploited to constrain the noise [45], [71], [72], [73], [74], [75]. The idea is to sample the SCN at the reference pixels with known displacement time series, interpolate it onto the PS locations and subtract the interpolated noise screen from the observations. In [71], [73], [74], and [75], the sampled SCN in interferograms was interpolated using different surface fitting approaches. We adapt the general approach by interpolating the noise, taking its spatial statistics into account. The approach shares the basic idea of the covariance-based InSAR and GNSS fusion method presented in [45]. Their method, however, is used to calibrate estimated displacement rates with GNSS measurements, taking the spatial statistics of the displacement rate error into account. Our approach aims at reducing SCN in single interferograms, thus reducing the uncertainty in the derived PS displacement time series. In the following, we assume that a phase-to-displacement conversion has already been carried out in the interferograms.

The flowchart of our proposed method to correct for residual SCN in single interferograms is displayed in Fig. 3. The first step is to sample the unknown interferogram SCN at reference pixels with known displacement time series. The ground truth displacement $d_{nk}^{\mathrm{gt}}$ of reference PS $k$ in an interferogram $n$ can be computed by subtracting the PS's ground truth position $\mathbf{r}_k(t)$ at the involved acquisitions $t_{n0}$ and $t_{n1}$ and projecting it onto the LOS of the SAR satellite

$$d_{nk}^{\mathrm{gt}} = [\mathbf{r}_k(t_{n0}) - \mathbf{r}_k(t_{n1})] \cdot \mathbf{e}_{\mathrm{los}}. \tag{1}$$

The SCN screen in an interferogram can then be sampled by calculating the residuals between the ground truth displacement and the interferogram LOS displacement at that position.

In the case of GNSS stations used as references, the residuals are commonly calculated between their displacement and the mean displacement of PSs located in a radius around them. If presumably stable regions are selected as reference, it is assumed that $d_{nk}^{\mathrm{gt}} = 0$, thus that the interferogram observations of PSs
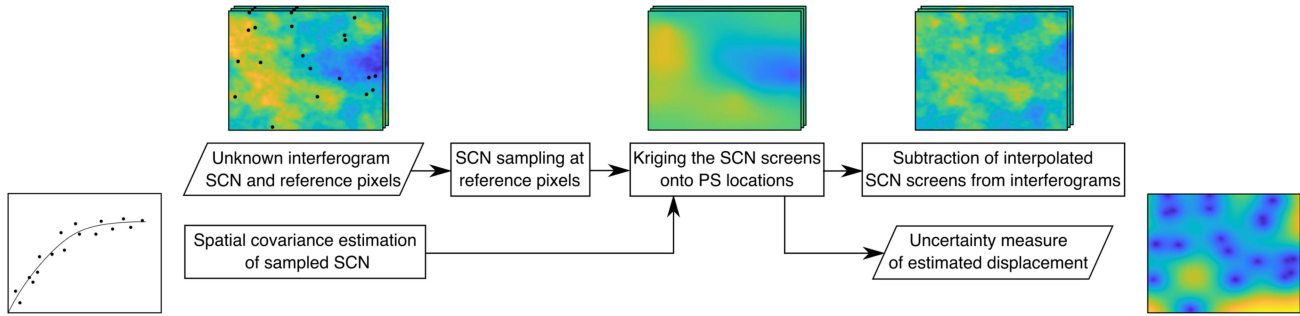
Fig. 3. Flowchart of the reference integration for residual SCN noise estimation in a stack of interferogram.

located in these regions equal the residual SCN. The unevenly sampled SCN is then interpolated, taking its spatial statistics into account, in order to get an estimate of the SCN screen at each PS location. The variance-covariance matrix $C_{\text{ref}}$ of the sampled SCN at $K$ reference pixels has to be estimated for this purpose, which is defined as

$$C_{\text{ref}} = \text{diag}\left\{\sigma_{\text{gt},1}^2, \ldots, \sigma_{\text{gt},K}^2\right\} + \text{diag}\left\{\sigma_{\text{PSI},1}^2, \ldots, \sigma_{\text{PSI},K}^2\right\}$$
$$+ C_{\text{scn}}\left(\mathbf{x}_{\text{ref}}, \mathbf{x}_{\text{ref}}\right) \qquad (2)$$

where $\sigma_{\text{gt},k}^2$ and $\sigma_{\text{PSI},k}^2$ denote the variances of the ground truth and PSI derived displacements, respectively, and $C_{\text{scn}}$ the covariance of the SCN at the reference PSs $\mathbf{x}_{\text{ref}}$. We implicitly assume in this definition that the variances $\sigma_{\text{gt}}^2$ and $\sigma_{\text{PSI}}^2$ are independent and not spatially correlated. The ground truth variance depends on which kind of reference is used. In case of GNSS stations being used as reference, the ground truth variance $\sigma_{\text{gt}}^2$ is the variance of their displacement estimates. For weekly solutions, this would be in the order of tens of mm$^2$. In contrast, the ground truth variance can be assumed to be zero if regions are selected as reference which are presumably stable during the study period. The variance of the PSI derived displacements of the reference PSs used to calculate the residuals between the ground truth and the PSI results can be estimated by means of their estimated temporal coherence. The variance also is in the order of tens of mm$^2$.

The covariance estimation of the residual SCN is carried out under the assumption of spatial stationarity after the subtraction of modeled tropospheric delays and tidally induced displacements. The same assumption was also made in [45] and [76]. In this case, the covariance matrix $C_{\text{scn}}(i, j)$ is only depending on the distance $\Delta_{ij}$ between PS pixels $i$ and $j$

$$C_{\text{scn}}(i, j) = C_{\text{scn}}(\Delta_{ij}) \qquad (3)$$

and can be described by the variogram $\Gamma(\Delta_{ij})$. In general, the number and spatial distribution of reference pixels across the study area are too poor for a robust estimation of the SCN variograms. Instead, we take the median of the variograms between all available PS pixels in many interferograms with small temporal baselines. The median variogram is automatically fitted with a variogram model, which represents the average covariance of the SCN in all interferograms. Interferograms with small temporal baselines are used to minimize displacement

induced phases of examined PS pixels which do not belong to the set of reference pixels, as done in [45]. The impact of potential high-magnitude displacement events on short time scales is suppressed by taking the median of the variograms in several interferograms.

The sampled SCN can be interpolated onto the PS locations using ordinary kriging as soon as its variance-covariance matrix has been estimated. The kriging method is, however, referred to as error cokriging since the measurement variances of the sampled SCN are considered in $C_{\text{ref}}$ [77] and [78]. The goal of the kriging interpolation is to invert the weights of the sampled SCN at each reference PS for the interpolation at each other PS location, taking its variance-covariance matrix into account. The interpolated SCN screen is finally subtracted from the interferograms to get the adjusted displacements.

One of the advantages of the proposed method, besides considering the spatial statistics during interpolation, is that the prediction variance–covariance of the interpolation is known. The variance at query point $x_0$ is given by

$$\sigma_{\text{ck}}^2(x_0) = \mu + C_{\text{scn}}(0) - \mathbf{w}^T C_{\text{scn}}\left(\mathbf{x}_{\text{ref}}, x_0\right) \qquad (4)$$

where $\mathbf{w}$ denotes the weight vector of the reference PSs for the interpolation at pixel $x_0$ and $\mu$ the Lagrange multiplier, which are simultaneously inverted during the kriging process by means of a least-squares inversion. The variance depends on the location of $x_0$ with regard to the reference pixels, the covariance of the SCN and the variances of the sampled SCN. For increasing measurement variances $\sigma_{\text{gt}}^2 + \sigma_{\text{PSI}}^2$ at all reference pixels with regard to the covariance of the SCN, the weights of the reference pixels increasingly align at each query point.

The prediction covariance between query points $x_0$ and $x_1$ with weight vectors $\mathbf{w_0}$ and $\mathbf{w_1}$ and Lagrange multipliers $\mu_0$ and $\mu_1$ is

$$C_{\text{ck}}(x_0, x_1) = \mu_1 + C_{\text{scn}}(\Delta_{x_0 x_1}) - \mathbf{w_1}^T C_{\text{scn}}\left(\mathbf{x}_{\text{ref}}, x_0\right)$$
$$= \mu_0 + C_{\text{scn}}(\Delta_{x_0 x_1}) - \mathbf{w_0}^T C_{\text{scn}}\left(\mathbf{x}_{\text{ref}}, x_1\right). \quad (5)$$

The equation elucidates that the residual noise in interferograms after subtraction of the interpolated SCN screens is no longer stationary, but has a covariance which is depending on the particular location of the considered pixels with regard to the reference PSs.
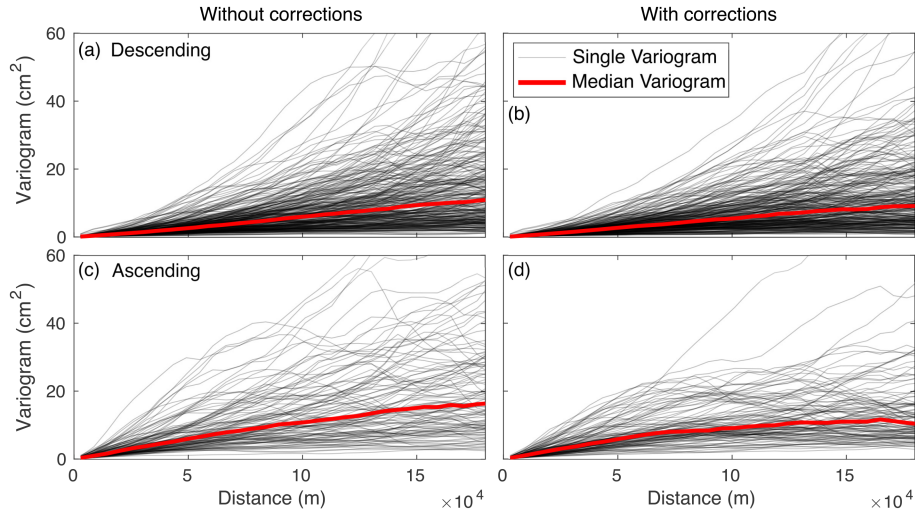
Fig. 4. Single and median variograms of interferograms with small temporal baselines before (a) and (c), and after geodetic corrections (b) and (d) in the descending (a) and (b) and ascending stack (c) and (d).

The consideration of the uncertainty propagation of the sampled SCN in the proposed referencing method allows to give an approximation of the final covariance matrix of the PSI derived displacement results of all $L$ pixels

$$\hat{C}_{\text{final}} = \text{diag}\left\{\sigma^2_{\text{PSI},1}, \ldots, \sigma^2_{\text{PSI},L}\right\} + C_{\text{ck}}. \qquad (6)$$

We refer to the diagonal of this matrix as the estimated displacement variance $\hat{\sigma}^2_d = \sigma^2_{\text{PSI}} + \sigma^2_{\text{ck}}$. The variances $\sigma^2_{\text{PSI}}$ could again be approximated based on the estimated temporal coherence of the pixels, for example. However, it has to be kept in mind that phase deviations from the functional model assumed in the PSI phase noise estimation step lead to inaccuracies in the temporal coherence estimation. Further inaccuracies in $\hat{C}_{\text{final}}$ are unconsidered unwrapping errors, a falsely assumed stationarity of the residual SCN and insufficient modeling of the spatial covariance based on the mean variogram of small-baseline interferograms.

In cases where displacement rates $v$ are estimated by means of a least-squares inversion, the variance of the displacement estimation can be used to derive the variance of the rate estimation $\sigma^2_v$ for each pixel using the following expression:

$$\hat{\sigma}^2_v = \left(A^T \hat{\sigma}^{-2}_d A\right)^{-1} \qquad (7)$$

where $A$ denotes the design matrix of the inversion which contains the temporal baselines of the interferogram network. Note that no temporal covariance is estimated or included in the stochastic model. The variance of the displacement rate estimation is underestimated when temporal correlations persist in the residual SCN.

### D. SCN Variograms

Variograms of interferograms with short temporal baselines before and after the geodetic corrections described in Section III-B are displayed in Fig. 4. The median variograms of interferograms without corrections approach 11.3 and 16.5 cm$^2$

at 180 km distances in the descending and ascending stack, respectively. Single variograms reach up to 135 cm$^2$ in both stacks at 180 km distance. The median variograms of interferograms after the corrections approach 9.4 and 11 cm$^2$, respectively, with single variograms reaching up to about 80 cm$^2$ in both stacks.

While the median variogram before and after the corrections is lower at all distances in the descending stack compared to the ascending stack, the gain provided by the corrections is larger in the ascending stack. The larger variogram values in the ascending stack are probably related to high water vapor content and variability at local acquisition time. Solar radiation leads to evaporation during the day, and the diurnal rain cycle in the rainy season is usually characterized by an increased frequency of rainfall events in the evening in the lower Mekong Basin [79]. Additionally, Liang et al. [80] showed that ionospheric effects on MT-InSAR can be strong for ascending data acquired in low-latitude areas such as the VMD, while descending data is largely unaffected. The different impact of the ionosphere on the stacks originates in the different acquisition times. However, a visual inspection of the interferograms revealed that the residual noise is mainly characterized by larger wavenumbers than expected from ionospheric delays. This led us to the conclusion that the residual noise in both stacks is mainly due to insufficient tropospheric delay modeling.

### E. Reference Area Selection

Displacement ground truth is sparse in the VMD. To our knowledge, there is only one permanent GNSS station located in Bac Lieu [81], whose data are not freely available. Measurements from repeated levelling campaigns are also not available. The only areas with presumably zero subsidence during the considered time period are solid rock outcrops located in the north-western part of the delta and a small outcrop island which is called Hon Da Bac and located at the western coast of the VMD. The spatial distribution of these outcrops is poor, and
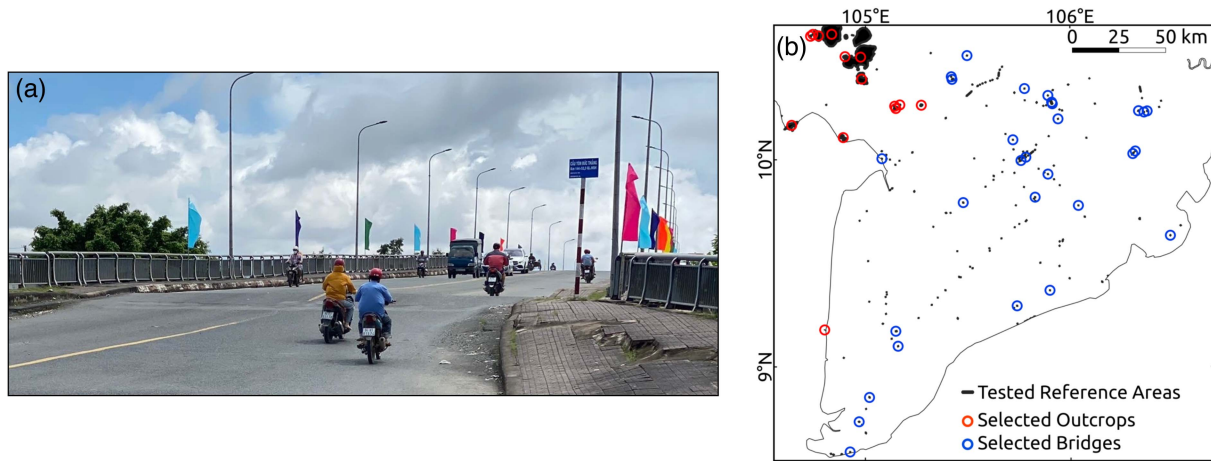
Fig. 5. (a) Photograph of a bridge in the VMD featuring the characteristic street bump at its border. (b) Tested and selected reference areas, including solid rock outcrops and large bridges.

there are pixels which are located more than 160 km away from the nearest outcrop. The variograms in Fig. 4 indicate that points at this distance are not spatially correlated, i.e., the application of the SCN kriging method from Section III-C will not improve the uncertainty of the estimated displacement at these pixels, compared to simply removing the mean phase of all pixels located on the outcrops.

For the mentioned reason, we selected additional reference PSs which are located on large bridges with lengths over 250 m. The motivation behind consists of several factors. First, large bridges feature deep piled foundations with a pile length of up to 73 m (personal communication from Renck, A., 2021), thus should be only affected by potential subsidence originating from deeper soil layers. Wit et al. [8] showed that buildings with pile foundations are more stable than their surroundings in three cities in the VMD, indicating a considerable contribution of shallow soil layer compaction to the total subsidence. The results coincide with the findings of [46] who studied differential subsidence between large bridges and their surroundings. The fact that many larger bridges are more stable than their surroundings can also be experienced in the field when driving by car onto the bridges. Their onset usually features a characteristic street bump, which has been caused by the bridge surroundings subsiding at a higher rate than the bridges themselves. An example of such a bump can be seen in Fig. 5(a).

Second, relative movements of the bridges at acquisition, e.g., induced by vehicle crossings, can be canceled out by averaging the sampled interferogram noise over multiple PSs distributed along the bridges. Residual relative movements as well as potential unmodeled thermally induced displacements lower the temporal coherence of PSs on the bridges. As a result, these effects are considered in the stochastic model of the noise screen estimation in the form of variances of the PSI derived displacements $\sigma_{\mathrm{PSI}}^2$ of the reference points (see Section III-C). However, we assume thermally induced displacements to be insignificant due to the low temperature variability in the VMD. The standard deviations of ERA-5 based temperatures at image acquisitions were 1.2 and 1.4 K in the city of Can Tho in the descending and ascending stack, respectively.

Solely subsidence above the foundation depth of the bridges can be measured if (T)PSs on selected bridges are selected as reference, with zero displacements assumed. However, bridges which are, potentially due to insufficient foundations, subsiding or tilting relatively to nearby bridges are identified in a triangulation network between all selected reference areas and a combination of ascending and descending stacks. They were removed from the set of reference bridges.

The location of bridges with lengths over 250 m was extracted from Open Street Map, and polygons were automatically created to represent the extent of the bridges, as described in [46]. For the selection of the final reference (T)PSs on the bridges, various statistical tests were carried out with the goals to: 1) identify and remove (T)PSs which are actually not located on the bridges or located on parts of the bridges which are actually moving over time; and 2) identify and remove bridges which are moving relatively due connected bridges in the triangulation network.

For the selection of the (T)PSs on each potential reference bridge, the median displacement time series of all (T)PSs within the particular bridge polygon was subtracted from the observations, and standard outlier tests based on the median absolute deviation (mad) were conducted to identify scatterers with abnormal relative displacement variance or displacement rate. The identification of subsiding or horizontally moving bridges was carried out in two steps. First, a separate triangulation network was spanned between all potential bridges and solid rock outcrops in both orbit stacks. The differential displacement time series along the edges of the network were then statistically analyzed. Edges which involved one or two moving bridges were detected with outlier tests comparing the sample with the predicted differential displacement and displacement rate variance for the given edge length. The latter were predicted based on the variance-covariance of the SCN (see Section III-C). Additionally, the Ljung-Box-test [82] was carried out to test if the differential displacement time series was stationary, i.e., did not exhibit significant autocorrelation, similarly to its application in [42]. The identified outlier edges were removed from the network, and isolated bridges were removed from the set of potential reference bridges.

TABLE I
NUMBER OF IDENTIFIED PSs, TPSs, AND SPECIFIC TPS TYPES IN THE
DESCENDING AND ASCENDING DATA STACKS

|  | Descending | Ascending |
|---|---|---|
| # PSs | 1 520 494 | 2 399 046 |
| # TPSs | 5 604 863 | 2 826 369 |
| # appearing TPSs | 2 445 395 | 1 685 026 |
| # fading TPSs | 1 135 846 | 766 210 |
| # visiting TPSs | 1 234 826 | 280 231 |
| # recurring TPSs | 739 564 | 94 902 |

TABLE II
STATISTICS OF THE ESTIMATED SUBSIDENCE RATES OF PSs IN THE
DESCENDING AND ASCENDING STACK FOR THE MEAN REFERENCING[1] AND
THE PROPOSED REFERENCING APPROACH[2]

|  | Desc.[1] | Asc.[1] | Desc.[2] | Asc.[2] |
|---|---|---|---|---|
| 5% Rate Prctile (mm/yr) | −0.1 | −4 | −0.6 | −1.2 |
| Median rate (mm/yr) | 9.4 | 7.1 | 8.2 | 7.5 |
| 95% rate Prctile (mm/yr) | 31.3 | 32.6 | 30.0 | 29.5 |
| Median rate Std. (mm/yr) | 1.2 | 2.0 | 0.3 | 0.6 |

Finally, another triangulation network was spanned between all remaining bridges and solid rock outcrops, which were included in both orbit data stacks. First, the LOS displacements were projected to the vertical, making use of the local incidence angle, assuming that displacements in the VMD are exclusively vertical, as also done in [20] and [22]. Then, the subsidence time series differences between both orbit stacks were computed along each edge and the previous tests were repeated in order to identify and remove horizontally moving bridges. The assumption behind was that the differential vertical displacement time series between bridges without horizontal movement should be similar in the ascending and descending stack. The final set of selected reference areas is displayed in Fig. 5. We assume the piled foundations of all used reference bridges to be about 70 m, due to their similar length and infrastructural purpose.

## IV. RESULTS AND DISCUSSION

### A. Identified Observation Points

The proposed algorithm identified 7 125 357 observation points in the descending stack, from which 1 520 494 and 5 604 863 are PSs and TPSs, respectively. In the ascending stack, 5 225 415 observation points were identified, which is the sum of 2 399 046 PSs and 2 826 369 TPSs. The breakdown of identified TPSs by TPS type is given in Table I. The share of appearing TPSs in the total number of identified TPSs is largest in both stacks, which is probably due to the high construction activity in the VMD. The ratio of identified TPSs to PSs in the descending stack is comparable with the findings in [43], which were based on descending data of six years length in the cities of Can Tho and Ca Mau and two rural areas in the VMD. The ratio differs in the ascending stack. We assume that the difference in the number of identified (T)PSs in both stacks is due to two reasons. First, the noise level in the ascending stack is on average higher than in the descending stack, which is described in Section III-D and potentially leads to a decreased number of identified observation points. Second, the ascending stack only consists of 115 SAR scenes with an average temporal difference of 15.8 days between consecutive scenes, compared to the descending stack, which consists of 277 scenes with an average temporal difference of 7 days between consecutive scenes. One processing parameter of the TPS identification is the minimum number of consecutive acquisitions that a TPS has to be coherent or incoherent in order that the change dates describing this segment can be identified. This parameter was set to 25 in the analysis. As a result, a coherent TPS segment has to be, on average, at least 395 days

in the ascending stack in order to be identifiable, compared to 175 days in the descending stack. About 1.3 million TPSs with a total coherent period of less than 395 days were identified in the descending stack. We assume that the different PS to TPS ratios in both stacks are also constituted in that fact, since TPSs with short incoherent segments are more likely to be falsely identified as PSs in the ascending stack compared to the descending stack.

### B. Overview of Estimated Subsidence

We here compare the estimated subsidence time series and rates of two different referencing methods: 1) referencing to the mean sampled SCN at all reference points in each interferogram, which is the standard referencing method in InSAR and, for example, implemented in the StaMPS algorithm; and 2) our proposed referencing method. The results by the mean referencing are mostly influenced by the reference pixels identified on the solid rock outcrops, since these make up about 85% of the total reference pixels in both orbit stacks. This also means that the center of gravity of the mean referencing approach is located in the north-western part of the study area, and that the results from that approach comprise the largest part of the absolute subsidence, including subsidence originating from below the foundation depth of the used reference bridges.

The estimated subsidence rates in both stacks derived from the two referencing methods are displayed in Fig. 6. Only PSs are displayed for the sake of consistency in the covered period. Furthermore, the points were thinned out to a maximum of 50 PSs per square kilometer and sorted the way that PSs with highest subsidence rates overlay those with lower rates in the visualization. It has to be kept in mind that the modeled phase noise components, comprising modeled tropospheric delays based on the ERA-5 reanalysis, tidally induced displacements and plate motion (see Section III-B), have been reduced from the observations in both results. The estimated standard deviations of the rate estimations, which were estimated with the method of bootstrapping, are also displayed for both referencing methods and orbits. Basic statistics of the displayed results are given in Table II.

The estimated rates are characterized by high spatial heterogeneity in all displayed results. Highest rates were mainly identified in populated areas like Can Tho and Bac Lieu, however also in various rural areas. Differences between gridded subsidence rates in both orbit stacks are displayed in Fig. 7 for both referencing approaches. The distribution of the differences between both orbit stacks for the mean referencing is right skewed, with a mean of −1.3 mm/yr. This is caused by long-wave differences,
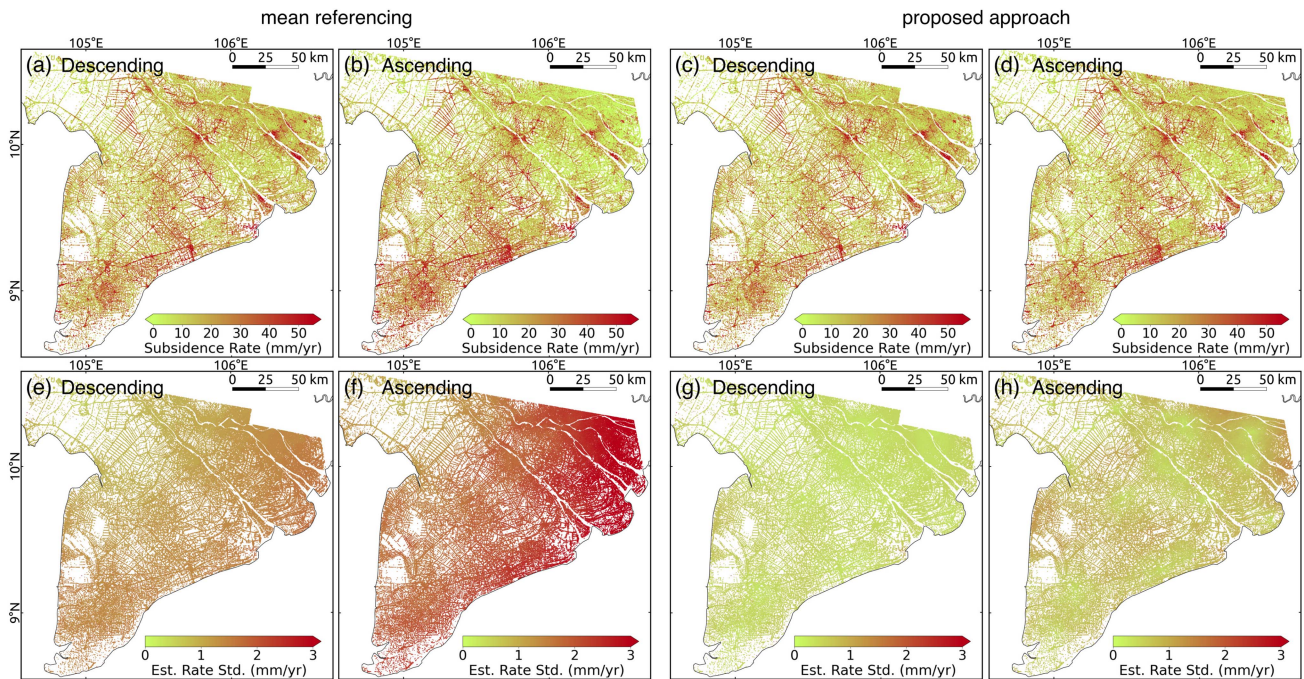
Fig. 6. Estimated subsidence rates (a)–(d) and estimated rate standard deviations (e)–(h) in both orbit stacks over the VMD for the mean referencing approach (a), (b), (e), (f) and our proposed referencing approach (c), (d), (g), and (h).

which manifest as a spatial ramp in SW-NE direction and ranges from about −10 mm/yr in the south–west to about 10 mm/yr in the north–east. There are two possible reasons behind this ramp. First, large scale horizontal movements could lead to differences in the estimated vertical displacement rates. However, we do not expect horizontal movements on that scale in a sedimentary delta after the reduction of plate motions from the observations. That's why we assume that the differences are due to spatially and temporary correlated noise in the displacement estimates, leading to biased subsidence rate estimates.

The 5% and 95% percentiles of the estimated subsidence rates for the mean referencing are −0.1 and 31.3 mm/yr in the descending and −4 and 32.6 mm/yr in the ascending stack, and the median rates are 9.4 and 7.1 mm/yr, respectively. The estimated negative subsidence rates at parts of the observation points suggest an uplift, which we do not expect in the area. This could be a result of residual temporally correlated SCN, unwrapping errors or large outliers, leading to a biased rate estimation. Horizontal movements of sporadic pixels towards the sensor also potentially contribute to this observation, e.g., caused by tilts of buildings. The median rate standard deviations are 1.2 and 2 mm/yr in both stacks for the mean referencing, respectively. The standard deviations are characterized by increasing values with increasing distance to the center of gravity of the reference network. The reason behind the higher standard deviations in the ascending compared to the descending results lies in the overall increased noise level in the ascending stack (see Fig. 4) and the considerable lower number of acquisitions in this stack compared to the descending stack.

The results in both orbit stacks agree to a much larger degree for our proposed referencing approach. The median subsidence

rates are 8.2 and 7.5 mm/yr in the descending and ascending stack, respectively. The 5% and 95% percentiles of the estimated subsidence rates are −0.6 and 30.0 mm/yr in the descending and −1.2 and 29.5 mm/yr in the ascending stack. The median rate standard deviations are 0.3 and 0.6 mm/yr, respectively. The rate standard deviations are lowest in the vicinity of the reference areas, as expected, and increase with increasing distance. The spatial trend in the differences between the results in both stacks is no longer present, and the differences are normally distributed with a mean of −0.4 mm/yr and a standard deviation of 4.8 mm/yr. We conclude that spatially and temporary correlated noise is effectively reduced in our proposed referencing method with the infrastructural reference network. Residual differences between the results in both stacks are possibly due to unwrapping errors, local horizontal movements and residual temporary correlated SCN at large distances from the reference network.

Vertical displacement time series at exemplary locations are compared in Fig. 7 for the two referencing methods. It is striking that the overall trend of the time series is similar in both methods, but the variance is considerably reduced in our proposed referencing method compared to the mean referencing. Furthermore, the time series of descending and ascending stacks agree to a much higher degree in our proposed approach. Here, nonlinear displacements can be identified with a considerably lower uncertainty. Furthermore, there are apparent nonlinear signals in the results from the mean referencing, which are removed in our proposed approach. For example, the time series in the descending stack at the first three locations feature seasonal undulations, which are not as clear in the ascending stack and almost completely removed in the results from our proposed approach. There are two possible reasons for the
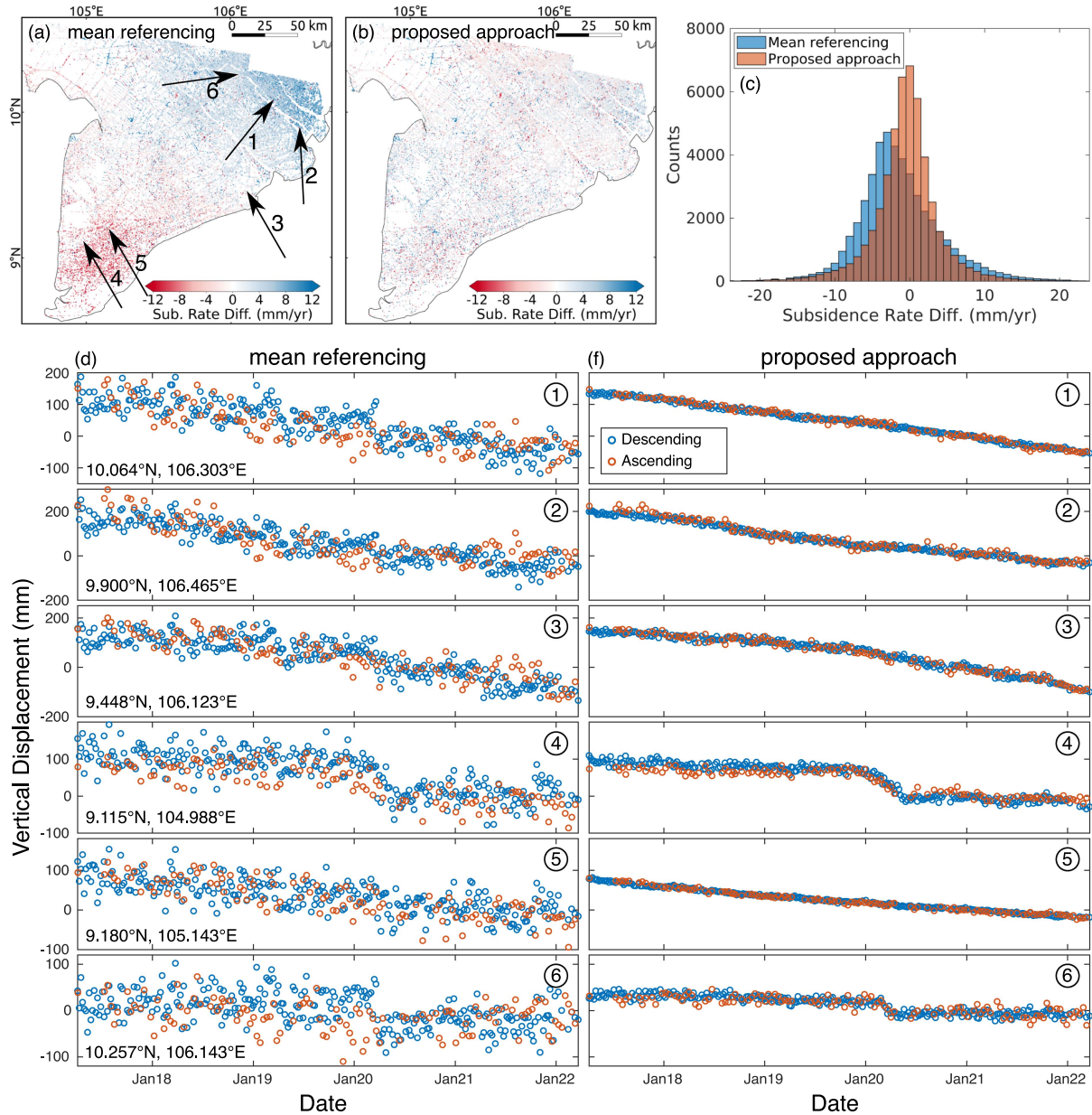
Fig. 7. Differences in gridded subsidence rates derived from the descending and ascending stacks for the mean referencing (a) and the proposed approach (b). (c) Histogram of the differences between the two approaches. Below: Mean subsidence time series, with respect to the master scenes, for all (T)PSs in a radius of 400 m around the six locations indicated by arrows in the upper left panel for both the mean referencing (d) and our proposed approach (f).

observed differences. First, it could be possible that there are undulating vertical displacements originating in depths below the foundation depth of the reference bridges, caused by seasonal undulations of groundwater levels in the aquifers below. In that case, these signals should be present in the results of the mean referencing method, since the set of reference pixels mostly consists of reference pixels located on the solid rock outcrops, as described before. However, the seasonal signals should be similar in the descending and ascending stacks. Furthermore, Duy et al. [83] studied the groundwater dynamics across the VMD and found that significant seasonal variations of groundwater levels in coastal areas are mainly found in the Holocene and upper Pleistocene aquifers, which are expected to

be located above the foundation depth of the bridges. We rather assume that the differences in both referencing approaches are due to seasonally correlated residual SCN in the results of the mean referencing at the eastern coast of the VMD, which is effectively reduced in our approach.

In general, various kinds of nonlinear subsidence are found in the VMD. Exemplary kinds can be identified based on the displayed time series in Fig. 7, including increasing subsidence rates (Location 3), decreasing subsidence rates (Location 5), short term rapid subsidence (Location 4/6), and continuously varying subsidence (Location 2). No consistent trend in temporal subsidence rate changes can be identified which is representative for the whole delta.
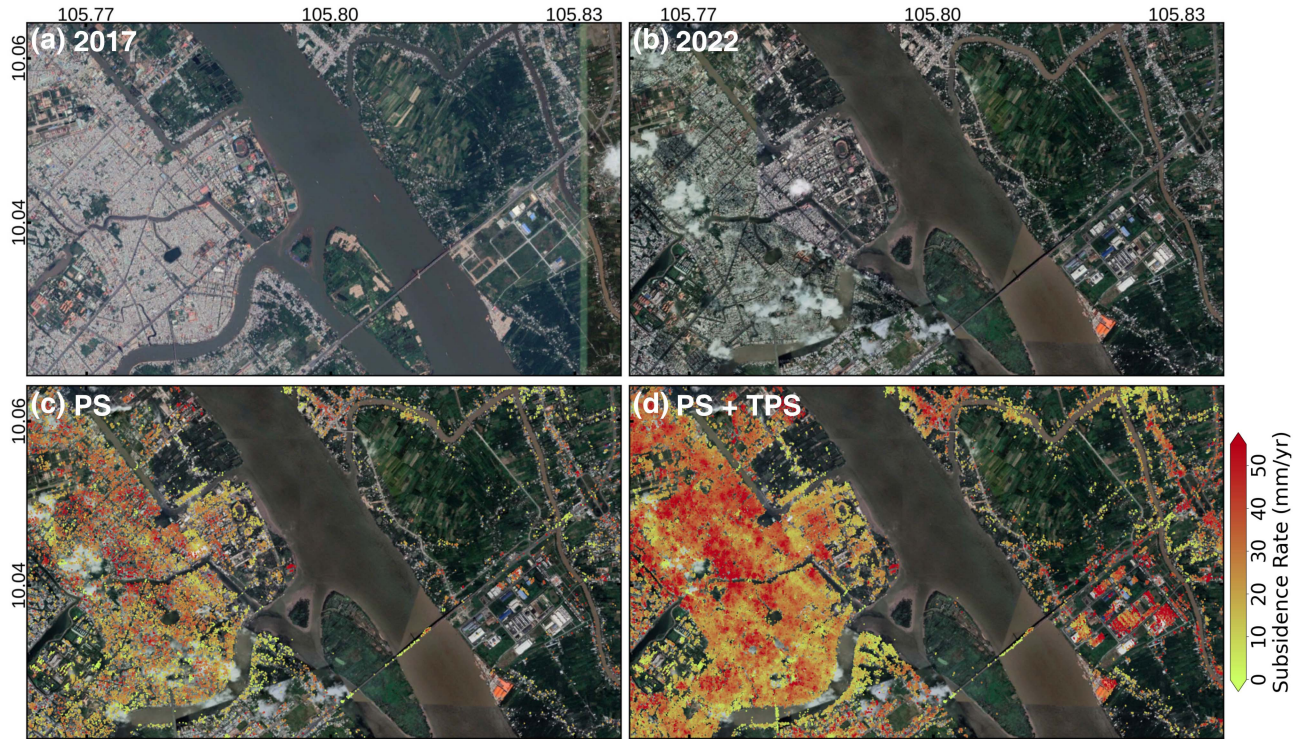
Fig. 8. Optical images of Can Tho city before and after the analyzed time series in 2017 (a) and 2022 (b), respectively. Estimated subsidence rates of PSs (c) and (T)PSs (d) in Can Tho. Imagery data: Google Earth, 2024 Maxar Technologies.

The difference in the median subsidence rates between the two referencing approaches is small. The median subsidence rate in the descending stack is only 1.2 mm/yr higher for the mean referencing compared to our proposed referencing approach, while the median subsidence rate in the ascending stack is even 0.4 mm/yr lower. We have discussed before that the results from the mean referencing approach comprises the largest part of the total subsidence, since most reference pixels are located on the solid rock outcrops, while the results of our proposed approach only include subsidence from above the foundation depth of the reference bridges in the largest part of the study area, which we assume to be about 70 m. Due to the small differences in the estimated rates between the two referencing approaches, we conclude that the largest part of the subsidence originates from depths above the foundation depth of the bridges. In-depth future research is necessary on the relation between the observed shallow land subsidence and groundwater extraction from different aquifers as well as load-induced and natural sediment compaction. This could be done, for example, by carrying out pumping tests from different aquifers, which are monitored by land subsidence observation wells that measure compaction in various sediment layers [84].

An exemplary zoom-in into the estimated subsidence rates in the city of Can Tho is displayed in Fig. 8, which moreover illustrates the impact of the TPS integration. The overall densification of the observation points provided by the TPS integration is significant, as already shown in [42]. At the same time, it becomes apparent that the TPS integration only leads to a higher point identification in the built-up areas. No TPSs were identified in vegetated areas, which underlines the robustness

of the approach. A striking area is located in the south-eastern part of the zoom-in, where industrial buildings were built during the analyzed time series. No PSs but many TPSs were identified in this area. In general, Fig. 8 highlights the large subsidence variability on short spatial scales. Subsidence rates in Can Tho reach from few mm/yr to about 9 cm/yr at short distances. The subsidence rates of PSs and TPSs agree very well.

### C. Comparison of Predicted and Estimated Rate Standard Deviations

The reference integration method proposed in Section III-C provides the predicted standard deviation of the subsidence time series, which can be used to predict the standard deviation of the subsidence rate estimation (7). Both measures are displayed in Fig. 9 for the results in the descending and ascending stacks. The predicted standard deviations are lowest in the vicinity of the reference areas and increase with increasing distance, like the estimated rate standard deviations displayed in Fig. 7. The median subsidence standard deviation is 7.7 and 11.5 mm in the descending and ascending stack, respectively, while the median subsidence rate standard deviation is 0.33 and 0.77 mm/yr. The histograms of the differences between the predicted rate standard deviations and those estimated with bootstrapping are also shown in Fig. 9. The median differences are 0.01 and 0.1 mm/yr, respectively, meaning that the predicted standard deviation are, on average, slightly larger than the estimated ones. On the other hand, both distributions of the differences are left skewed, which is caused by nonlinear subsidence of
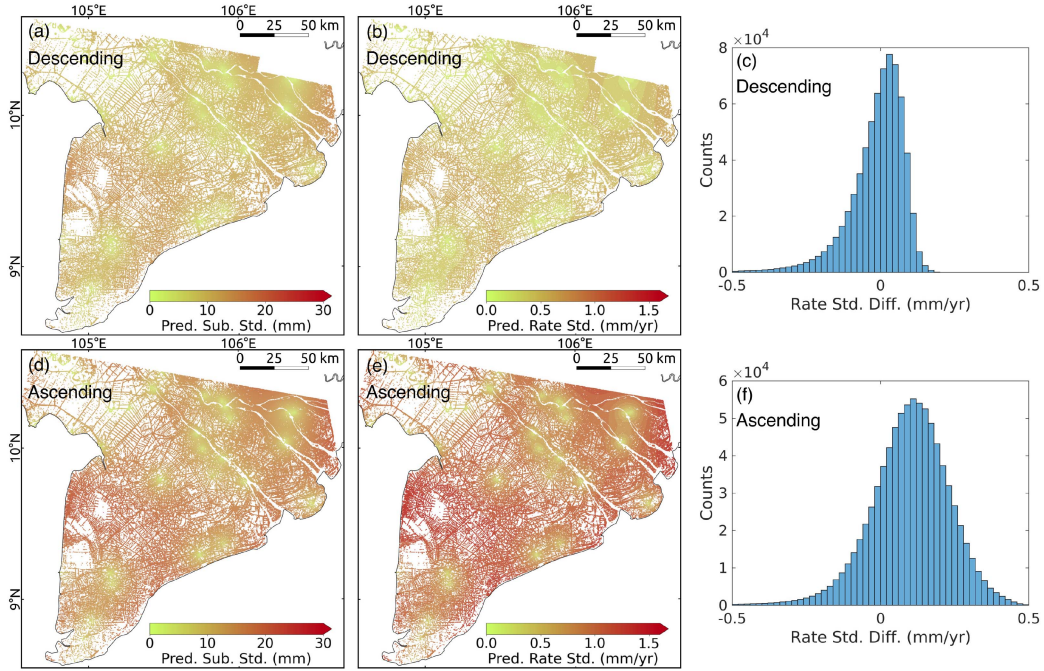
Fig. 9.    (a) Predicted subsidence standard deviation, (b) predicted subsidence rate standard deviation, and (c) histogram of differences between predicted and estimated subsidence rate standard deviations in the descending stack. (d)–(f) same as (a)–(c) in the ascending stack.

(T)PSs, which is not considered in the standard deviation predictions.

We consider the predicted and estimated rate standard deviations to be in good agreement. We conclude that the proposed referencing method provides the possibility to predict the displacement time series and rate standard deviations across a study area, based on an available reference network and knowledge of the spatial statistics of the SCN, even before the MT-InSAR analysis is carried out. This way, the feasibility of an MT-InSAR study with predefined uncertainty levels can be evaluated in a preliminary study, without having to run the whole MT-InSAR processing. In case that the opportunity exists to densify the reference network, e.g., by installing new permanent GNSS stations in the study area, the method can be used to find the optimal number and locations of additional reference objects to finally achieve a specified uncertainty level with the MT-InSAR study.

### D. Validity of Stationarity Assumption

Depending on the study area, the assumption of spatial and temporal stationarity of the SCN should be questioned. The application of kriging with temporary and/or spatially variable variograms [85] could improve the SCN interpolation and prediction of the interpolation variances in certain study areas. We tested seasonally and spatially variable variogram selections and carried out the kriging interpolation of the sampled phases at the selected reference objects in the small-baseline interferograms, which were used for the variogram averaging in Fig. 4 and assumed to be dominated by SCN. We checked the root-mean-square-error of the interpolation and variance prediction and did not find an improvement in the interpolation and

variance prediction performance over simply using the median variogram.

## V. CONCLUSION

We presented land subsidence time series and rates in the VMD based on descending and ascending Sentinel-1 data, which was acquired between April 2017 and April 2022. We applied an advanced PSI approach that fully integrates TPSs and is able to optimally integrate reference points with known displacement time series to suppress residual SCN. While the optimal reference network would be a dense network of permanent GNSS stations, we here exploited solid rock outcrops and large bridges with deep piled foundations as references, due to a lack of GNSS stations in the study area. This way, only subsidence originating from soil layers above the foundation depth of the bridges, which is approximately 70 m, could be measured in large parts of the study area. However, we discussed that virtually the whole measured subsidence originates from shallower layers. Future research on the relation between groundwater extraction from aquifers at various depths and the identified shallow subsidence is needed.

The algorithm identified a high density of observation points across the study area. Considerably more TPSs than PSs were identified in both stacks. The results confirm the applicability of the proposed TPS integration method in [42] in large scale investigations. The estimated subsidence rates are characterized by a large spatial variability on short and large spatial scales across the study area, with the largest rates mainly identified in urban areas. The median subsidence rates are 8.2 and 7.5 mm/yr and the 95% rate percentiles are 30 and 29.5 mm/yr in the descending and ascending stack, respectively. We compared the

proposed referencing approach with the standard mean referencing to reference pixels, after reduction of modeled tropospheric delays and phases due to tidal and plate motion, and showed that the variances of the estimated subsidence are considerably decreased by our method, enabling the robust study of nonlinear motions on short temporal scales. Residual temporary correlated SCN can also be effectively reduced with the method.

We showed that the method allows to preliminarily evaluate the feasibility of an MT-InSAR study with specified uncertainty levels, given an available reference network and knowledge of the spatial statistics of the SCN in the study area. Conversely, it can be used to design a reference network with an aspired uncertainty level for displacement estimates.

The retrieved subsidence time series can be exploited for in-depth studies of the causes of land subsidence in the Mekong Delta. For example, they can serve as input into hydrogeological models or can be examined with regard to correlations to groundwater extraction rates, land cover, and use, as well as climatological data. The data is accessible at.[1]

## REFERENCES

[1] D. L. Galloway and T. J. Burbey, "Review: Regional land subsidence accompanying groundwater extraction," *Hydrogeol. J.*, vol. 19, no. 8, pp. 1459–1486, 2011.

[2] F. G. Bell, T. R. Stacey, and D. D. Genske, "Mining subsidence and its effect in the environment: Some differing examples," *Environ. Geol.*, vol. 40, no. 1/2, pp. 135–152, 2000.

[3] J. C. Stephens, L. H. Allen, and E. Chen, "Organic soil subsidence," *GSA Rev. Eng. Geol.*, vol. 6, pp. 107–122, 1984.

[4] J. D. Martinez, K. S. Johnson, and J. T. Neal, "Sinkholes in evaporite rocks," *Amer. Scientist*, vol. 86, no. 1, pp. 38–51, 1998.

[5] T. A. Meckel, U. S. ten Brink, and S. J. Williams, "Current subsidence rates due to compaction of Holocene sediments in southern Louisiana," *Geophysical Res. Lett.*, vol. 33, no. 11, pp. 1–5, 2006.

[6] F. E. Nelson, O. A. Anisimov, and N. I. Shiklomanov, "Subsidence risk from thawing permafrost," *Nature*, vol. 410, no. 6831, pp. 889–890, 2001.

[7] N. Phien-wej, P. H. Giao, and P. Nutalaya, "Land subsidence in Bangkok, Thailand," *Eng. Geol.*, vol. 82, no. 4, pp. 187–201, 2006.

[8] K. de Wit et al., "Identifying causes of urban differential subsidence in the Vietnamese Mekong Delta by combining InSAR and field observations," *Remote Sens.*, vol. 13, no. 2, pp. 1–33, 2021.

[9] N. C. Don, N. T. M. Hang, H. Araki, H. Yamanishi, and K. Koga, "Salinization processes in an alluvial coastal lowland plain and effect of sea water level rise," *Environ. Geol.*, vol. 49, no. 5, pp. 743–751, 2006.

[10] A. Smajgl et al., "Responding to rising sea levels in the Mekong Delta," *Nature Climate Change*, vol. 5, no. 2, pp. 167–174, 2015.

[11] H. Z. Abidin, H. Andreas, I. Gumilar, and I. R. Wibowo, "On correlation between urban development, land subsidence and flooding phenomena in Jakarta," *IAHS-AISH Proc. Rep.*, vol. 370, pp. 15–20, 2015.

[12] M. M. Miller and M. Shirzaei, "Land subsidence in Houston correlated with flooding from Hurricane Harvey," *Remote Sens. Environ.*, vol. 225, pp. 368–378, 2019, doi: 10.1016/j.rse.2019.03.022.

[13] B. Tellman et al., "Satellite imaging reveals increased proportion of population exposed to floods," *Nature*, vol. 596, no. 7870, pp. 80–86, 2021, doi: 10.1038/s41586-021-03695-w.

[14] L. Zou, J. Kent, N. S. Lam, H. Cai, Y. Qiang, and K. Li, "Evaluating land subsidence rates and their implications for land loss in the lower Mississippi River Basin," *Water (Switzerland)*, vol. 8, no. 1, pp. 1–15, 2016.

[15] D. A. Edmonds, R. L. Caldwell, E. S. Brondizio, and S. M. Siani, "Coastal flooding will disproportionately impact people on river deltas," *Nature Commun.*, vol. 11, no. 1, pp. 1–8, 2020, doi: 10.1038/s41467-020-18531-4.

[16] J. P. Syvitski et al., "Sinking deltas due to human activities," *Nature Geosci.*, vol. 2, no. 10, pp. 681–686, 2009, doi: 10.1038/ngeo629.

[17] C. Tay et al., "Sea-level rise from land subsidence in major coastal cities," *Nature Sustainability*, vol. 5, no. 12, pp. 1049–1057, 2022.

[18] R. J. Nicholls et al., "A global analysis of subsidence, relative sea-level change and coastal flood exposure," *Nature Climate Change*, vol. 11, no. 4, pp. 338–342, 2021, doi: 10.1038/s41558-021-00993-z.

[19] A. Aobpaet, M. C. Cuenca, A. Hooper, and I. Trisirisatayawong, "InSAR time-series analysis of land subsidence in Bangkok, Thailand," *Int. J. Remote Sens.*, vol. 34, no. 8, pp. 2969–2982, 2013.

[20] L. E. Erban, S. M. Gorelick, and H. A. Zebker, "Groundwater extraction, land subsidence, and sea-level rise in the Mekong Delta, Vietnam," *Environ. Res. Lett.*, vol. 9, no. 8, 2014, Art. no. 084010.

[21] K. Karlsrud, L. Tunbridge, N. Q. Khanh, and N. Q. Dinh, "Preliminary results of land subsidence monitoring in the Ca Mau Province," *Proc. Int. Assoc. Hydrological Sci.*, vol. 382, pp. 111–115, 2020.

[22] P. S. Minderhoud, I. Hlavacova, J. Kolomaznik, and O. Neussner, "Towards unraveling total subsidence of a mega-delta-the potential of new PS InSAR data for the Mekong Delta," in Proc. Int. Assoc. Hydrological Sci., 2020, vol. 382, pp. 327–332.

[23] D. Hak et al., "Spatio-temporal variations of sea level around the Mekong Delta: Their causes and consequences on the coastal environment," *Hydrological Res. Lett.*, vol. 10, no. 2, pp. 60–66, 2016.

[24] P. S. Minderhoud, L. Coumou, G. Erkens, H. Middelkoop, and E. Stouthamer, "Mekong Delta much lower than previously assumed in sea-level rise impact assessments," *Nature Commun.*, vol. 10, no. 1, pp. 1–13, 2019, doi: 10.1038/s41467-019-11602-1.

[25] T. L. Cosslett and P. D. Cosslett, *Water Resources and Food Security in the Vietnam Mekong Delta*. Berlin, Germany: Springer, 2014.

[26] S. E. Darby et al., "Fluvial sediment supply to a mega-delta reduced by shifting tropical-cyclone activity," *Nature*, vol. 539, no. 7628, pp. 276–279, 2016, doi: 10.1038/nature19809.

[27] G. M. Kondolf, Z. K. Rubin, and J. T. Minear, "Dams on the Mekong: Cumulative sediment starvation," *Water Resour. Res.*, vol. 50, no. 6, pp. 5158–5169, 2014.

[28] E. J. Anthony, G. Brunier, M. Besset, M. Goichot, P. Dussouillez, and V. L. Nguyen, "Linking rapid erosion of the Mekong River delta to human activities," *Sci. Rep.*, vol. 5, pp. 1–12, 2015, doi: 10.1038/srep14745.

[29] J. L. Gunnink, H. V. Pham, G. H. Oude Essink, and M. F. Bierkens, "The three-dimensional groundwater salinity distribution and fresh groundwater volumes in the Mekong Delta, Vietnam, inferred from geostatistical analyses," *Earth Syst. Sci. Data*, vol. 13, no. 7, pp. 3297–3319, 2021.

[30] S. Eslami et al., "Dynamics of salt intrusion in the Mekong Delta: Results of field observations and integrated coastal-inland modelling," *Earth Surf. Dyn.*, vol. 9, no. 4, pp. 953–976, 2021.

[31] P. S. Minderhoud et al., "Impacts of 25 years of groundwater extraction on subsidence in the Mekong Delta, Vietnam," *Environ. Res. Lett.*, vol. 12, no. 6, 2017, Art. no. 064006.

[32] C. Zoccarato, P. S. Minderhoud, and P. Teatini, "The role of sedimentation and natural compaction in a prograding delta: Insights from the mega Mekong Delta, Vietnam," *Sci. Rep.*, vol. 8, no. 1, pp. 1–12, 2018, doi: 10.1038/s41598-018-29734-7.

[33] P. S. Minderhoud, L. Coumou, L. E. Erban, H. Middelkoop, E. Stouthamer, and E. A. Addink, "The relation between land use and subsidence in the Vietnamese Mekong Delta," *Sci. Total Environ.*, vol. 634, pp. 715–726, 2018, doi: 10.1016/j.scitotenv.2018.03.372.

[34] T. V. Hoan, K. G. Richter, N. Börsig, J. Bauer, N. T. Ha, and S. Norra, "An improved groundwater model framework for aquifer structures of the quaternary-formed sediment body in the southernmost parts of the Mekong Delta, Vietnam," *Hydrol.*, vol. 9, no. 4, 2022, Art. no. 61. [Online]. Available: https://www.mdpi.com/2306-5338/9/4/61

[1][Online]. Available: https://doi.org/10.35097/YYpQiWnfZaqMVybS

[35] F. Wagner, V. B. Tran, and F. G. Renaud, "Groundwater resources in the Mekong Delta: Availability, utilization and risks," *Mekong Delta Syst.*, pp. 201–220, 2012. [Online]. Available: https://link.springer.com/book/10.1007/978-94-007-3962-8

[36] L. E. Erban, S. M. Gorelick, H. A. Zebker, and S. Fendorf, "Release of arsenic to deep groundwater in the Mekong Delta, Vietnam, linked to pumping-induced land subsidence," *Proc. Nat. Acad. Sci. United States Amer.*, vol. 110, no. 34, pp. 13751–13756, 2013. [Online]. Available: https://link.springer.com/book/10.1007/978-94-007-3962-8

[37] H. T. Pham, W. Rühaak, V. Schuster, and I. Sass, "Fully hydro-mechanical coupled plug-in (SUB) in FEFLOW for analysis of land subsidence due to groundwater extraction," *SoftwareX*, vol. 9, pp. 15–19, 2019.

[38] J. Bauer, N. Börsig, V. C. Pham, T. V. Hoan, H. T. Nguyen, and S. Norra, "Geochemistry and evolution of groundwater resources in the context of salinization and freshening in the southernmost Mekong Delta, Vietnam," *J. Hydrol.: Regional Stud.*, vol. 40, 2022, Art. no. 101010.

[39] V. T. Danh and H. V. Khai, "Household demand and supply for clean groundwater in the Mekong Delta, Vietnam," *Renewables: Wind, Water, Sol.*, vol. 2, no. 1, 2015, Art. no. 4.

[40] A. Ferretti, C. Prati, and F. Rocca, "Permanent scatterers in SAR interferometry," *IEEE Trans. Geosci. Remote Sens.*, vol. 39, no. 1, pp. 8–20, 2001.

[41] M. Crosetto, O. Monserrat, M. Cuevas-González, N. Devanthéry, G. Luzi, and B. Crippa, "Measuring thermal expansion using X-band persistent scatterer interferometry," *ISPRS J. Photogrammetry Remote Sens.*, vol. 100, pp. 84–91, 2015, doi: 10.1016/j.isprsjprs.2014.05.006.

[42] N. Dörr, A. Schenk, and S. Hinz, "Fully integrated temporary persistent scatterer interferometry," *IEEE Trans. Geosci. Remote Sens.*, vol. 60, 2022, Art. no. 4412815. [Online]. Available: https://ieeexplore.ieee.org/document/9862970/

[43] N. Dörr, A. Schenk, and S. Hinz, "On the relevance of temporary persistent scatterers for long-term PS-InSAR monitoring," in *Proc. Eur. Conf. Synthetic Aperture Radar*, Leipzig, 2022, pp. 541–546.

[44] A. Parizzi, R. Brcic, and F. De Zan, "InSAR performance for large-scale deformation measurement," *IEEE Trans. Geosci. Remote Sens.*, vol. 59, no. 10, pp. 8510–8520, Oct. 2021.

[45] A. Parizzi, F. R. Gonzalez, and R. Brcic, "A covariance-based approach to merging InSAR and GNSS displacement rate measurements," *Remote Sens.*, vol. 12, no. 2, 2020, Art. no. 300.

[46] N. Dörr, A. Schenk, and S. Hinz, "Analysis of heterogeneous PS-InSAR derived subsidence rates using categorized gis objects - a case study in the Mekong Delta," in *Proc. Int. Geosci. Remote Sens. Symp.*, 2021, pp. 2655–2658.

[47] P. Rizzoli et al., "Generation and performance assessment of the global TanDEM-X digital elevation model," *ISPRS J. Photogrammetry Remote Sens.*, vol. 132, pp. 119–139, 2017, doi: 10.1016/j.isprsjprs.2017.08.008.

[48] N. K. Pavlis, S. A. Holmes, S. C. Kenyon, and J. K. Factor, "The development and evaluation of the earth gravitational model 2008 (EGM2008)," *J. Geophysical Res.: Solid Earth*, vol. 117, no. 4, pp. 1–38, 2012.

[49] N. Yague-Martinez, F. De Zan, and P. Prats-Iraola, "Coregistration of interferometric stacks of Sentinel-1 TOPS data," *IEEE Geosci. Remote Sens. Lett.*, vol. 14, no. 7, pp. 1002–1006, Jul. 2017.

[50] F. Hu, J. Wu, L. Chang, and R. F. Hanssen, "Incorporating temporary coherent scatterers in multi-temporal InSAR using adaptive temporal subsets," *IEEE Trans. Geosci. Remote Sens.*, vol. 57, no. 10, pp. 7658–7670, Oct. 2019.

[51] C. W. Chen and H. A. Zebker, "Two-dimensional phase unwrapping with use of statistical models for cost functions in nonlinear optimization," *J. Opt. Soc. Amer. A*, vol. 18, no. 2, 2001, Art. no. 338.

[52] A. Hooper, P. Segall, and H. Zebker, "Persistent scatterer interferometric synthetic aperture radar for crustal deformation analysis, with application to Volcán Alcedo, Galápagos," *J. Geophysical Res.: Solid Earth*, vol. 112, no. 7, pp. 1–21, 2007.

[53] H. A. Zebker, P. A. Rosen, and S. Hensley, "Atmospheric effects in interferometric synthetic aperture radar surface deformation and topographic maps," *J. Geophysical Res.: Solid Earth*, vol. 102, no. B4, pp. 7547–7563, 1997.

[54] R. F. Hanssen, T. M. Weckwerth, H. A. Zebker, and R. Klees, "High-resolution water vapor mapping from interferometric radar measurements," *Science*, vol. 283, no. 5406, pp. 1297–1299, 1999.

[55] R. Hanssen, *Data Interpretation and Error Analysis*. Dordrecht, Netherlands: Kluwer Academic, 2001, vol. 91. [Online]. Available: https://www.amazon.com/Radar-Interferometry-Interpretation-Analysis-Processing/dp/0792369459

[56] H. Fattahi and F. Amelung, "InSAR uncertainty due to orbital errors," *Geophysical J. Int.*, vol. 199, no. 1, pp. 549–560, 2014.

[57] C. J. Dicaprio and M. Simons, "Importance of ocean tidal load corrections for differential InSAR," *Geophysical Res. Lett.*, vol. 35, no. 22, pp. 1–5, 2008.

[58] W. Peng, Q. Wang, F. B. Zhan, and Y. Cao, "Spatiotemporal ocean tidal loading in InSAR measurements determined by kinematic PPP solutions of a regional GPS network," *IEEE J. Sel. Topics Appl. Earth Observ. Remote Sens.*, vol. 13, pp. 3772–3779, 2020.

[59] H. Bähr, S. Samiei-Esfahany, and R. F. Hanssen, "On the effect of reference frame motion on InSAR deformation estimates," in *Proc. Fringe 2011 Workshop*, 2012.

[60] O. L. Stephenson, Y.-K. Liu, Z. Yunjun, M. Simons, P. Rosen, and X. Xu, "The impact of plate motions on long-wavelength InSAR-derived velocity fields," *Geophysical Res. Lett.*, vol. 49, no. 21, 2022, Art. no. e2022GL099835, doi: 10.1029/2022GL099835.

[61] Z. Hu and J. J. Mallorquí, "An accurate method to correct atmospheric phase delay for InSAR with the ERA5 global atmospheric model," *Remote Sens.*, vol. 11, no. 17, 2019, Art. no. 1969.

[62] D. Milbert, "Solid earth tide," 2018. [Online]. Available: https://geodesyworld.github.io/SOFTS/solid.htm

[63] D. C. Agnew, "SPOTL: Some programs for ocean-tide loading," Scripps Inst. Oceanography, SIO Tech. Rep., 2012. [Online]. Available: http://igppweb.ucsd.edu/agnew/Spotl/spotlman.pdf

[64] D. F. Argus, R. G. Gordon, and C. Demets, "Geologically current motion of 56 plates relative to the no-net-rotation reference frame," *Geochemistry, Geophys., Geosystems*, vol. 12, no. 11, pp. 1–13, 2011.

[65] S. Liu, R. Hanssen, and Á. Mika, "On the value of high-resolution weather models for atmospheric mitigation SAR interferometry," in *Proc. IEEE Int. Geosci. Remote Sens. Symp.*, 2009, pp. II-749–II-752.

[66] X. Cong, U. Balss, F. R. Gonzalez, and M. Eineder, "Mitigation of tropospheric delay in SAR and InSAR using NWP data: Its validation and application examples," *Remote Sens.*, vol. 10, no. 10, 2018, Art. no. 1515.

[67] M. E. Pritchard, M. Simons, P. A. Rosen, S. Hensley, and F. H. Webb, "Co-seismic slip from the 1995 Jul . 30 Mw = 8.1 Antofagasta, Chile, earthquake as constrained by InSAR and GPS observations," *Geophysical J. Int.*, vol. 150, no. 2, pp. 362–376, 2002.

[68] T. Fournier, M. E. Pritchard, and N. Finnegan, "Accounting for atmospheric delays in InSAR data in a search for long-wavelength deformation in south America," *IEEE Trans. Geosci. Remote Sens.*, vol. 49, no. 10 PART 2, pp. 3856–3867, Oct. 2011.

[69] W. Gong, F. J. Meyer, S. Liu, and R. F. Hanssen, "Temporal filtering of InSAR data using statistical parameters from NWP models," *IEEE Trans. Geosci. Remote Sens.*, vol. 53, no. 7, pp. 4033–4044, Jul. 2015.

[70] M. P. Doin, C. Lasserre, G. Peltzer, O. Cavalié, and C. Doubre, "Corrections of stratified tropospheric delays in SAR interferometry: Validation with global atmospheric models," *J. Appl. Geophys.*, vol. 69, no. 1, pp. 35–50, 2009, doi: 10.1016/j.jappgeo.2009.03.010.

[71] D. F. Argus, M. B. Heflin, G. Peltzer, F. Crampé, and F. H. Webb, "Interseismic strain accumulation and anthropogenic motion in metropolitan Los Angeles," *J. Geophysical Res.: Solid Earth*, vol. 110, no. 4, pp. 1–26, 2005.

[72] P. Lundgren, E. A. Hetland, Z. Liu, and E. J. Fielding, "Southern San Andreas-San Jacinto fault system slip rates estimated from earthquake cycle models constrained by GPS and interferometric synthetic aperture radar observations," *J. Geophysical Res.: Solid Earth*, vol. 114, no. 2, pp. 1–18, 2009.

[73] W. R. Neely, A. A. Borsa, and F. Silverii, "GInSAR: A cGPS correction for enhanced InSAR time series," *IEEE Trans. Geosci. Remote Sens.*, vol. 58, no. 1, pp. 136–146, Jan. 2020.

[74] X. Xu, D. T. Sandwell, E. Klein, and Y. Bock, "Integrated Sentinel-1 InSAR and GNSS time-series along the San Andreas fault system," *J. Geophysical Res.: Solid Earth*, vol. 126, no. 11, pp. 1–14, 2021.

[75] Y. Liu, G. Wang, X. Yu, and K. Wang, "Sentinel-1 InSAR and GPS-Integrated long-term and seasonal subsidence monitoring in Houston, Texas, USA," *Remote Sens.*, vol. 14, no. 23, 2022, Art. no. 6184.

[76] F. R. Gonzalez, A. Parizzi, and R. Brcic, "Evaluating the impact of geodetic corrections on interferometric deformation measurements," in *Proc. Eur. Conf. Synthetic Aperture Radar*, 2018, pp. 377–381.

[77] J. P. Chilès and P. Delfiner, *Geostatistics: Modeling Spatial Uncertainty in Probability and Statistics.*, 2nd ed., Hoboken, NJ, USA: Wiley, 2012.

[78] J. P. Chilès and N. Desassis, "Fifty years of Kriging," in *Handbook of Mathematical Geosciences: Fifty Years of IAMG*. Berlin, Germany: Springer, 2018, pp. 589–612.

[79] T. Kumiko, M. Takao, and M. Toru, "Seasonal changes in radiation and evaporation implied from the diurnal distribution of rainfall in the lower mekong," *Hydrological Processes*, vol. 22, no. 9, pp. 1257–1266, 2008.

[80] C. Liang, P. Agram, M. Simons, and E. J. Fielding, "Ionospheric correction of InSAR time series analysis of C-band Sentinel-1 TOPS data," *IEEE Trans. Geosci. Remote Sens.*, vol. 57, no. 9, pp. 6755–6773, Sep. 2019.

[81] D. T. Vu, S. Bruinsma, S. Bonvalot, D. Remy, and G. S. Vergos, "A quasigeoid-derived transformation model accounting for land subsidence in the Mekong Delta towards height system unification in Vietnam," *Remote Sens.*, vol. 12, no. 5, pp. 1–21, 2020.

[82] G. M. Ljung and G. E. Box, "On a measure of lack of fit in time series models," *Biometrika*, vol. 65, no. 2, pp. 297–303, 1978.

[83] N. L. Duy et al., "Groundwater dynamics in the Vietnamese Mekong Delta: Trends, memory effects, and response times," *J. Hydrol.: Regional Stud.*, vol. 33, no. Oct. 2020, Art. no. 100746, doi: 10.1016/j.ejrh.2020.100746.

[84] W. C. Hung et al., "Land subsidence in Chiayi, Taiwan, from compaction well, leveling and ALOS/PALSAR: Aquaculture-induced relative sea level rise," *Remote Sens.*, vol. 10, no. 1, 2018, Art. no. 40.

[85] P. Harris, M. Charlton, and A. S. Fotheringham, "Moving window Kriging with geographically weighted variograms," *Stochastic Environ. Res. Risk Assessment*, vol. 24, no. 8, pp. 1193–1209, 2010.

**Nils Dörr** received the B.Sc. degree in geophysics from the Institute of Geophysics, Karlsruhe Institute of Technology, Karlsruhe, Germany, in 2016, the M.Sc. degree in geophysics from the Institute of Geoscience, University of Kiel, Kiel, Germany in 2019, and the Ph.D. degree in geodesy from Karlsruhe Institute of Technology, in 2023.

He currently is with the Institute of Photogrammetry and Remote Sensing, Karlsruhe Institute of Technology. His current research interests include SAR interferometry and land subsidence.

**Andreas Schenk** received the diploma degree in applied geophysics from TU Berlin, Berlin, Germany, and the Ph.D. degree in geodesy from the Geodetic Institute, Karlsruhe Institute of Technology, Karlsruhe, Germany, in 2015.

Since 2015, he has been with the Institute of Photogrammetry and Remote Sensing, Karlsruhe Institute of Technology. His current research interests include remote sensing methods and the retrieval of geophysical variables from hyperspectral and radar remote sensing.

**Stefan Hinz** received the Ph.D. degree and venia legendi (Habilitation) degree in computer vision and remote sensing from the Technical University of Munich, Munich, Germany, in 2003 and 2008, respectively.

In 2008, he became a Full Professor and Director of the Institute of Photogrammetry and Remote Sensing with the Karlsruhe Institute of Technology, Karlsruhe, Germany. His research interests include theory and methods of computer vision and remote sensing, with particular focus on semantic image understanding, image sequence analysis, hyperspectral, and radar remote sensing.